H2020 FET-Open Research and Innovation Actions Project Number 766566
Antiferromagnetic spintronics (ASPIN)

Work package 2, Deliverable D2.2: Report on switching by THz and fs-optical pulses.

This report summarizes the work of the ASPIN project consortium on switching of antiferromagnets by THz and fs-optical pulses. We also give references to our corresponding publications containing additional information. The teams' contributions to this work were as follows:

- Institute of Physics in Prague (IOP): Materials growth and characterization, device fabrication, electrical measurements
- University of Nottingham (NOT): Materials growth and characterization, magnetic imaging
- Max-Planck Institutes (MPG): THz experiments, theory
- IGS Ltd. (IGS): Assessment of application potential
- Charles University in Prague (CHU): Optical measurements
- Johannes Gutenberg University in Mainz (JGU): Theory

Contents

1 Switching by THz-pulses **1**
1.1 Experimental setup 1
1.2 THz writing speed experiments 2
1.3 Determination of THz writing current and energy density 3

2 Switching by optical fs-pulses **8**

1 Switching by THz-pulses

1.1 Experimental setup

To establish the feasibility of extending the writing speed in antiferromagnets to the THz band, we compare our ps writing pulse experiments to the results obtained with longer writing pulses in the same device structure. Electron micrographs of the device are shown in Fig. 1. We first recall the previously established technique that has enabled the scaling of the writing pulse time τ_p down to 250 ps, corresponding to the writing speed $1/\tau_p$ of up to 4 GHz [1, 2] (see Report 1.3). In this scheme, the current pulses are delivered via wire-bonded contacts, and here $\tau_p \sim 100$ ps is at the limit achievable with common current-pulse setups. A reversible switching is realized in cross-shape bit cells (see Figs. 1) by alternating current pulses along one of the two orthogonal directions, as illustrated by white dashed lines on the electron microscopy image of the cell in Fig. 2A. Apart from the reversible switching controlled by alternating the two orthogonal writing currents, earlier studies have also shown that multiple-pulses can be applied successively along one writing path, revealing a multi-level switching characteristics naturally occurring in antiferromagnetic microstructures [3, 2, 4]. This has been associated with multi-domain reconfigurations [5], and we exploit the feature also in our ps-pulse experiments described below.

For our experiments with $1/\tau_p$ in the THz range, we use the same cross-shape bit cell and an analogous experimental setup. However, as illustrated in Fig. 2C, we employ a non-contact technique for generating the ultra-short current pulses in the memory cell to overcome the above limit of common contact-based current-pulse setups. To explore reversible writing with pulses of $\tau_p \approx 1$ ps, we apply free-space THz electro-magnetic pulses whose linear polarization can be chosen along two orthogonal

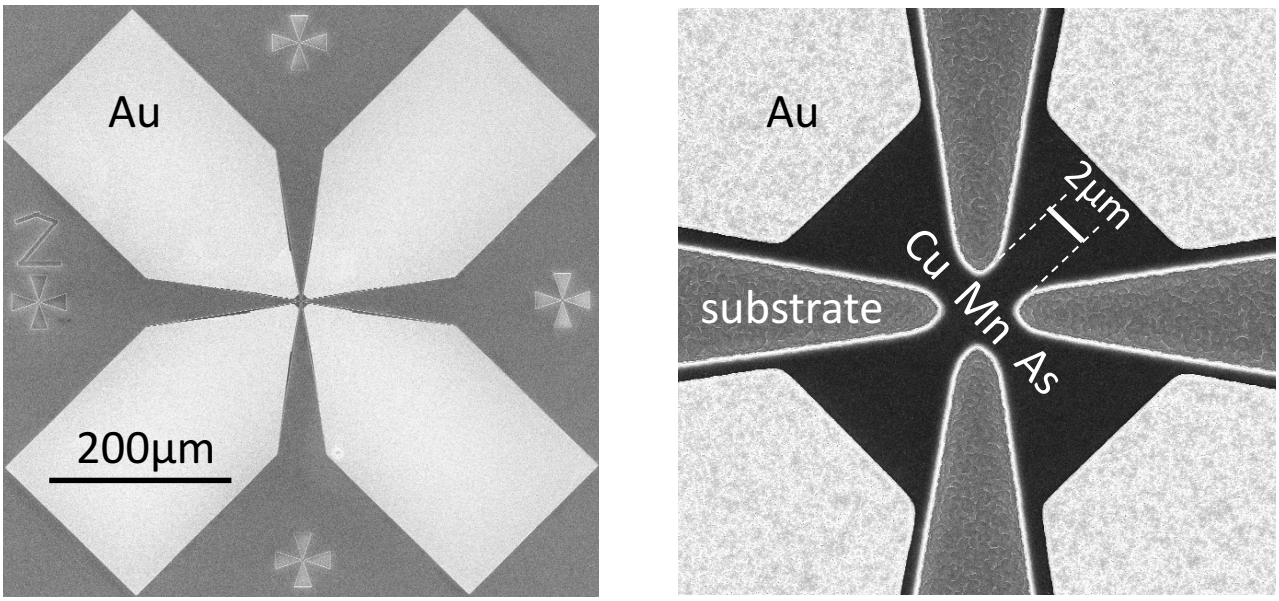

Figure 1: Left: Electron microscopy image of the Au-contact pads (light regions) of the device. Right: Detailed electron microscopy image of the device with a 2 μm size central cross struture. Light regions are the apices of Au-contact pads, grey regions are etched down to the GaAs substrate, and black regions are CuMnAs.

directions, as sketched in Fig. 2C. The wave-form of the incident electric-field transient is plotted in Fig. 2D [6]. In both contact and non-contact setups, the electrical readout is performed by detecting the transverse resistance (using a readout current amplitude of 3×10^5 Acm^{-2}), as illustrated in Fig. 3. Here the readout current direction is depicted by a white dashed line on the electron microscopy image of the cell. We applied a bipolar wave-form of the writing pulses also in the contact set-up to explicitly highlight the correspondence to the non-contact, ps-pulse measurements (cf. Figs. 2B,D). All experiments are performed at room temperature.

1.2 THz writing speed experiments

In Fig. 3A we first present measured data for μs writing pulses delivered by the contact method in a bit cell fabricated from a 50 nm thick CuMnAs film deposited on an insulating GaAs substrate. The pulse-train of one current-direction is turned on for 30 s, then the train is turned off for 30 s followed by turning on for 30 s the pulse-train with the orthogonal current direction. The data show the phenomenology attributed in the earlier studies to the multi-level switching of the antiferromagnet. The readout signal increases as the successive pulses within a train arrive at the bit-cell. The trend reverses when applying the pulse-train with the orthogonal current direction and, as expected, the overall sign of these reversible switching traces flips between the two readout geometries.

Note that the readout signal in Fig. 3A partially relaxes after turning the pulse-train off; the temperature dependent relaxation is discussed in detail in Report 1.3. Data in Fig. 3A were obtained for an applied writing current density $j = 3 \times 10^{7}$ $^{-2}$ and a writing pulse repetition rate of 1 Hz. More systematic dependencies of the switching signal on the writing pulse length, repetition rate, and current density in the contact set-up are in Report 1.3 and in Refs. [3, 2].

Analogous reversible switching traces, with an initial steep increase of the signal followed by a tendency to saturate, can be written in the same CuMnAs memory cell structure by ps-pulses, as shown in Fig. 3B. Here the current density, recalculated from the applied intensity of the THz electric-field $E = 1.1 \times 10^5$ Vcm^{-1}, was increased to $j \approx 2.7 \times 10^9$ Acm^{-2} for these ultra-short pulses. (The E to j conversion is discussed in detail below.) Note that this switching mechanism allows us

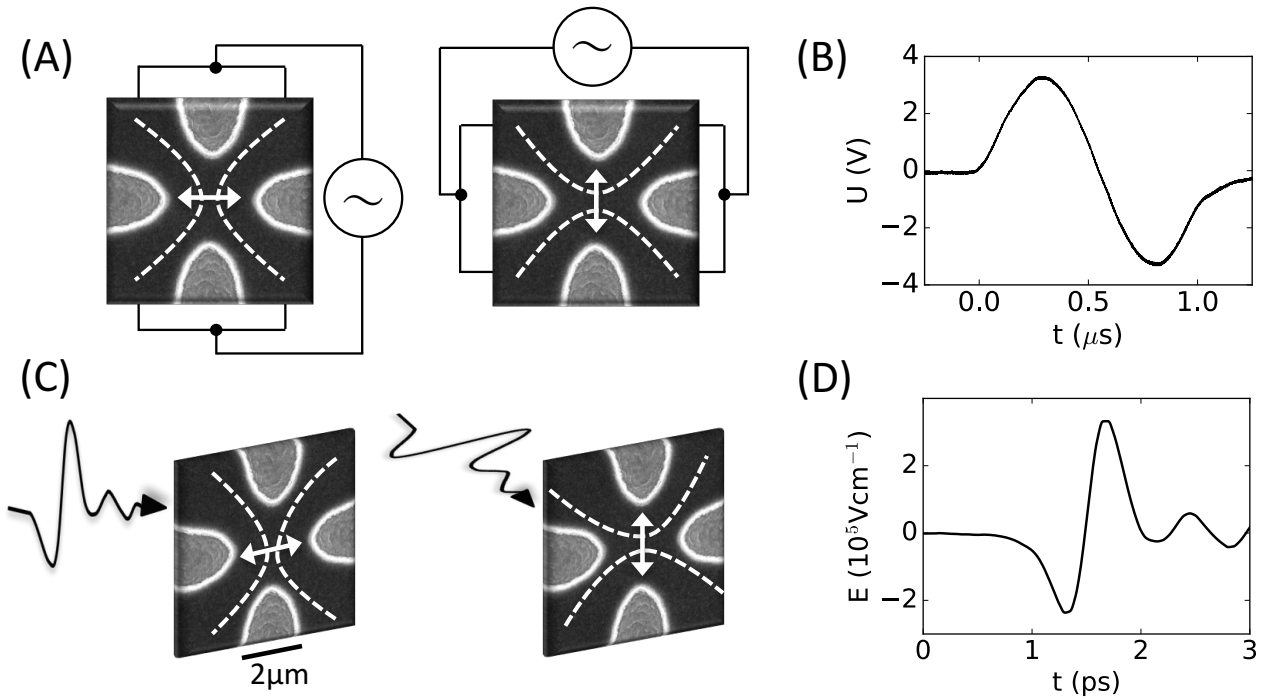

Figure 2: (A) Electron microscopy image of the cross-shape bit cell and schematics of the reversible writing by electrical pulses of two orthogonal current directions delivered via wire-bonded contacts. White dashed lines illustrate electrical current paths. (White double-arrows would correspond to preferred Néel vector orientations due to staggered current-induced spin-orbit field.) (B) Wave-form of the applied μs electrical pulses. (C) Schematics of the reversible writing by THz electric-field transients whose linear polarization can be chosen along two orthogonal directions. (D) Wave-form of the applied ps radiation pulses.

to employ the electric-field transient and that we do not rely on the weak magnetic-field component of the radiation [7], or on non-linear orbital-transition effects [8].

Performing a measurement with an isolated single-pulse was not feasible in our THz set-up. However, we emphasize that the writing pulse repetition rate in Fig. 3B was set to 1 kHz, i.e., the ratio of pulse-delay to pulse-length is as larger as 10^9. We also point out that at the millisecond (or longer) range of delays between writing pulses, the change of the signal due to the subsequent pulse in the train is not affected by, e.g., transient heating effects of the previous pulse and is independent of the delay time [2].

Still, to more explicitly highlight the effect of a single ps-pulse, we increased the current density to $j \approx 2.9 \times 10^9$ Acm^{-2} and further reduced the repetition rate of the writing pulses to 125 Hz and matched it closely to the readout repetition rate (100 Hz). The measured data plotted as a function of the pulse number are shown in Fig. 4A. We observe that the initial ps-pulse accounts for a sizable portion of the total signal generated by the pulse-train. (Note that the scatter in the measured data is likely of an instrumental origin due to the electrical noise from the laser setup and fluctuations of laser power and beam pointing.) In Fig. 4B we show corresponding measurements with the μs-pulses which again highlight the analogous phenomenology of the THz-speed writing and the slower writing in the multi-level antiferromagnetic bit cell.

1.3 Determination of THz writing current and energy density

The electrical current density generated in our CuMnAs memory cells for a given incident THz field could not be directly measured. To obtain the writing current density in the THz experiments,

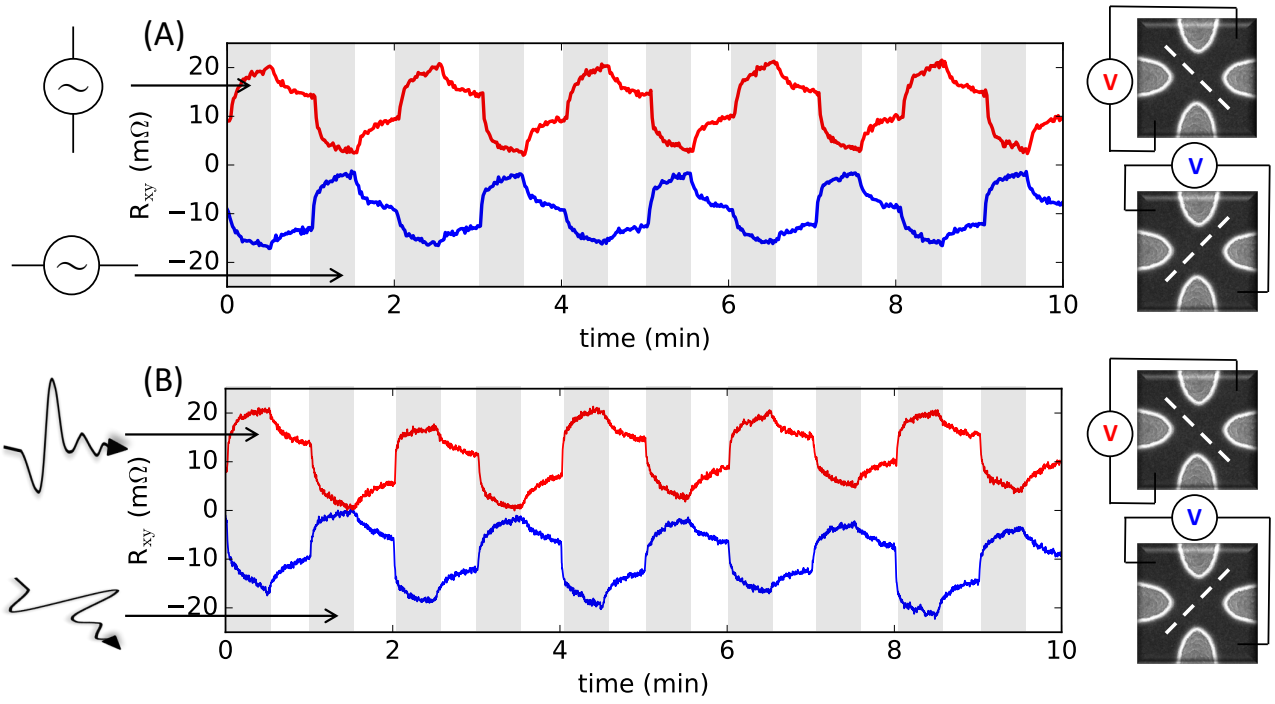

Figure 3: (A) Reversible multi-level switching by 30 s trains of μs electrical pulses with a Hz pulse-repetition rate, delivered via wire-bonded contacts along two orthogonal directions. The applied writing current density in the 3.5 μm-size CuMnAs/GaAs cell is 3×10^7 Acm^{-2}. Intervals with the pulse trains turned on are highlighted in grey and the two orthogonal current-directions of the trains are alternating from one interval to the next. Electrical readout is performed at a 1 Hz rate. Right insets show schematics of the transverse AMR readout. White dashed lines depict readout current paths. (B) Same as (A) for ps-pules with a kHz pulse-repetition rate. The writing current density in the 2 μm-size CuMnAs/GaAs bit cell recalculated from the amplitude of the applied THz electric-field transient is 2.7×10^9 Acm^{-2}. Electrical readout is performed at a 8 Hz rate.

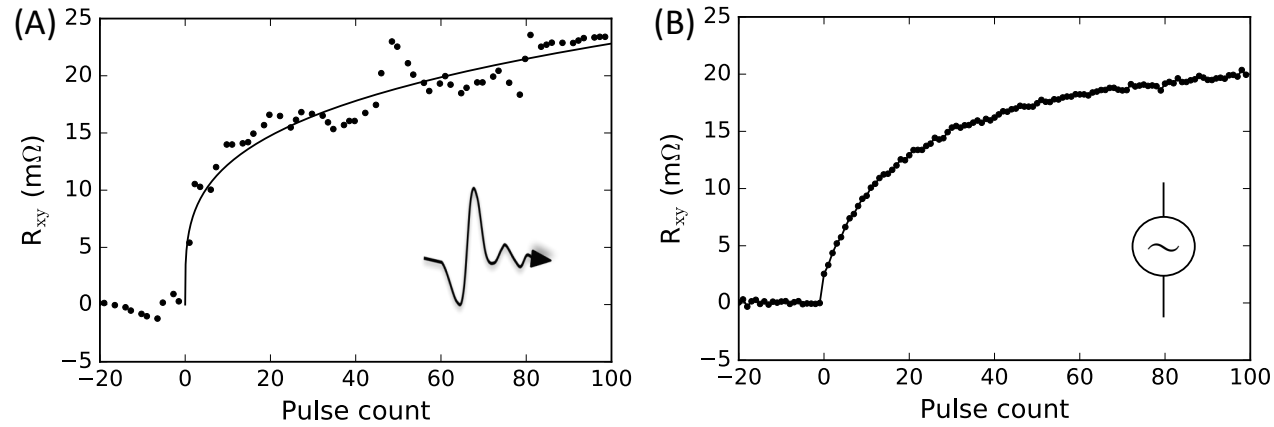

Figure 4: (A) The multi-level memory signal as a function of the number of applied ps-pulses. The writing current density in the 2 μm-size CuMnAs/GaAs bit cell recalculated from the applied THz field amplitude is 2.9×10^9 Acm^{-2}. (B) Same as (A) for the μs-pulses and an applied writing current density of 3×10^7 Acm^{-2} in the 3.5 μm-size CuMnAs/GaAs cell.

and the corresponding Joule energy density, we performed independent numerical simulations and experimental calibration based on sample breakdown measurements. These two alternative theoretical and experimental methods, that we now describe in more detail, provide quantitatively consistent results.

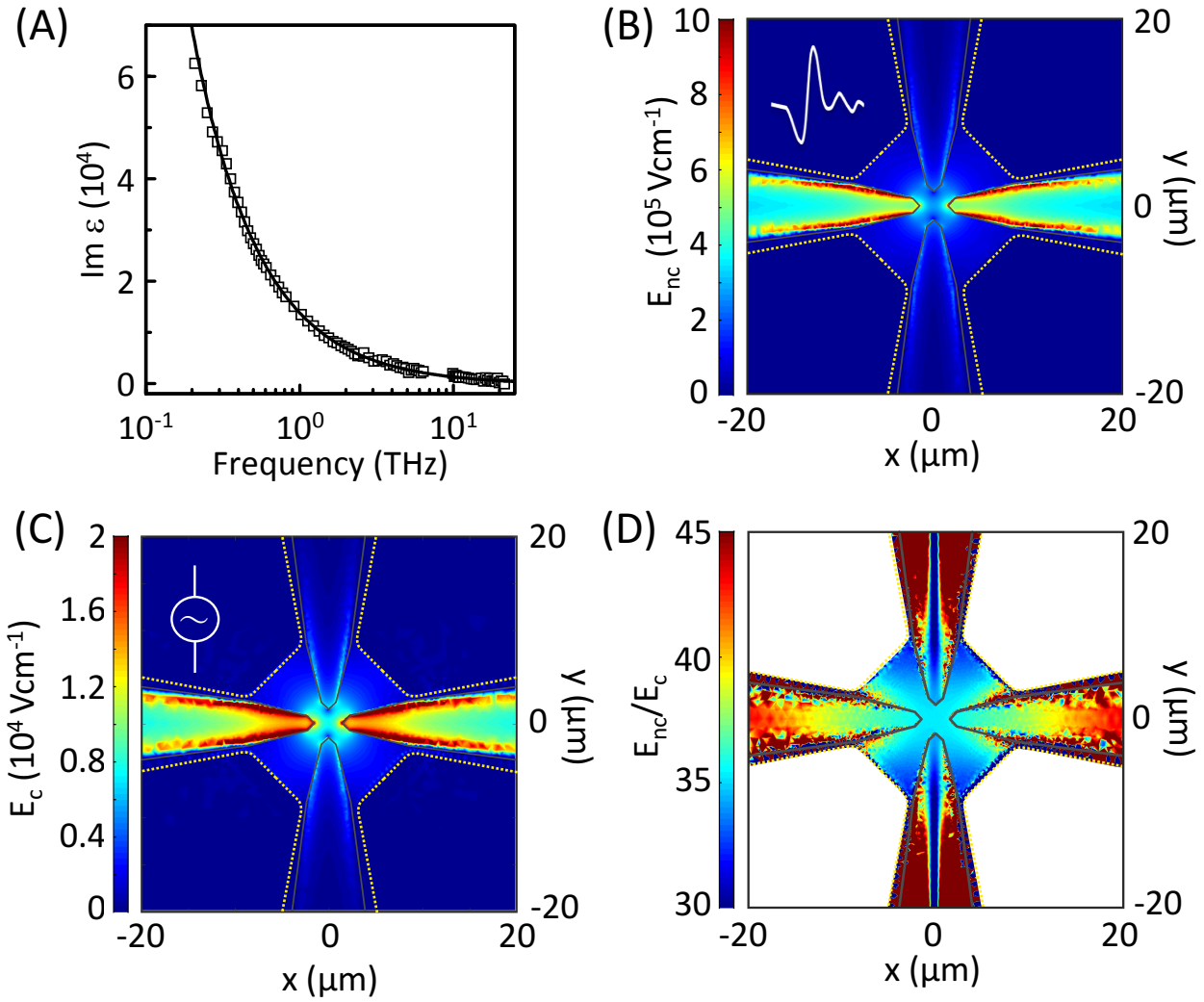

Figure 5: (A) Measured frequency-dependent imaginary part of the dielectric function (squares) and fitted expression $\mathrm{Im}\,\varepsilon = \sigma_0/\omega\varepsilon_0$ (line) with the dc conductivity $\sigma = 8 \times 10^3\ \Omega^{-1}\mathrm{cm}^{-1}$. (B) Numerical simulation of the electric field distribution in the device in the non-contact set-up for a peak incident THz field of 10^5 Vcm^{-1} polarized along the y-axis. (D) Same as (C) in the contact set-up for a voltage of 7 V applied between the top and bottom Au-contacts. (D) Ratio of the electric fields in panels (B) and (C).

The key input parameter of the numerical simulations is the frequency dependent dielectric function ε of CuMnAs whose measurement is shown in Fig. 5A. The data can be accurately fitted with $\mathrm{Im}\,\varepsilon = \sigma/\omega\varepsilon_0$ where the value of the dc conductivity $\sigma = 8\times10^3\ \Omega^{-1}\mathrm{cm}^{-1}$ agrees with the value obtained from electrical measurements. Using a transfer matrix formalism we first calculated the electric field inside the 50 nm thick CuMnAs layer in a layered structure of air/CuMnAs/GaAs without Au-electrodes upon incidence of the THz field. The amplitude of the electric field in CuMnAs is only 10% of the incident THz field value. For the peak incident THz field of 10^5 Vcm^{-1}, the calculated current density in the CuMnAs film would be 8×10^7 Acm^{-2}. Experimentally, we did not observe switching by the

THz-field pulses in structures without Au-electrodes which implies that this current density is below the switching threshold for ps-pulses.

Switching was observed in devices with Au-electrodes which strongly modify the incident THz field in the CuMnAs cross region. This is confirmed by numerical simulations of the THz electric field distribution that also took the measured dielectric function of CuMnAs at 1 THz frequency as an input and whose results are plotted in Figs. 5B,C. Here we compare, side by side, the electric field distribution in the cross structure for the typical peak incident THz field of 10^5 Vcm^{-1} used in the non-contact ps-pulse experiment (Fig. 5B) with the field distribution for the typical voltage of 7 V applied in the contact set-up for ns switching pulses (Fig. 5C). For clarity, we also plot in Fig. 5D the ratio of the fields in the two set-ups. The corresponding current densities in the center of the CuMnAs cross are $\approx 2 \times 10^9$ Acm^{-2} and 6×10^7 Acm^{-2}, respectively, which implies that the simulated writing energy density, $\epsilon = j^2 \tau_p / \sigma$, remains constant when increasing the writing speed $1/\tau_p$ from GHz to THz.

We now proceed to the experimental calibration of the writing current and energy density in the THz-field experiments. First we show in Figs. 6A,B measurements in devices with the width of the central cross of 1, 2, and 3 μm, and with otherwise the same geometry of the Au-electrodes (Fig. 6A) and approximately the same resistance of the devices. The THz-induced switching signal plotted as a function of the incident THz peak field depends on the size of the cross (Fig. 6B). We again ascribe this observation to the Au-electrodes. As shown previously in Ref. [9, 10], and consistent with the above simulations in Fig. 5B, a THz field polarized parallel to the electrode drives currents inside the metal, thereby inducing charges of opposite sign on opposite electrode apexes. These charges, and the resulting voltage across the inner device, govern the current in our CuMnAs crosses. At a given incident THz peak field, the current flowing through the three different crosses is comparable and, correspondingly, the current density scales up with decreasing width of the crosses. This is consistent with our observation of increasing AMR signal with decreasing cross size (Fig. 6B). Indeed, when we accordingly rescale the data in Fig. 6B by the cross sizes, as shown in the inset, the three curves fall on top of each other, in agreement with the expected phenomenology for the current-induced switching.

We point out that charges at the electrode apexes are induced also when a voltage is applied between opposite electrodes in the contact experiments. Therefore, similar field distributions in the cross region are formed for the contact and non-contact field applications, differing only by a global scaling factor. This is confirmed by our simulations in Fig. 5. We take advantage of this notion to experimentally calibrate the THz current. We determine in the contact experiments the critical absorbed Joule energy density leading to device damage for $1/\tau_p$ up to 4 GHz. Since the energy already saturates in the GHz range, extrapolation to the THz writing speed is straightforward and enables determination of the scaling factor between the incident peak field and the resulting peak current density in the CuMnAs cross.

The calibration procedure allows us to plot the characteristic Joule energy density ϵ required to obtain a reference switching signal of, e.g., 1 mΩ up to the THz range, as shown in the inset of Fig. 6C. We find a steeply decreasing ϵ with increasing $1/\tau_p$ below $\sim$MHz to a saturated value of ϵ in the GHz range (see also main plot of Fig. 6C) that extends to the THz writing speed. This demonstrates that, in agreement with the above numerical simulations, current-induced switching at the THz writing speed is as energy-efficient as at the GHz speed. (Note that a small increase of the writing current amplitude induces a large increase of the signal, as illustrated in Fig. 6B; our conclusions on the writing energy are therefore independent of the particular choice of the reference signal.)

The Joule energy leading to device damage and the energy required for switching are separated by approximately a factor of 2 in both the GHz and THz writing-speed range. The vicinity of the breakdown condition in our switching experiments is favorable from the perspective of the above current calibration procedure because it limits potential inaccuracies of the procedure. Simultaneously, the breakdown margin is sufficiently large, allowing us to demonstrate tens of thousands of reversible write-read cycles without any notable wear-out of our experimental devices [2].

In Fig. 6D we finally demonstrate that one antiferromagnetic multi-level bit-cell can be simultaneously addressed by the non-contact THz-speed writing and the contact lower-speed writing. For the

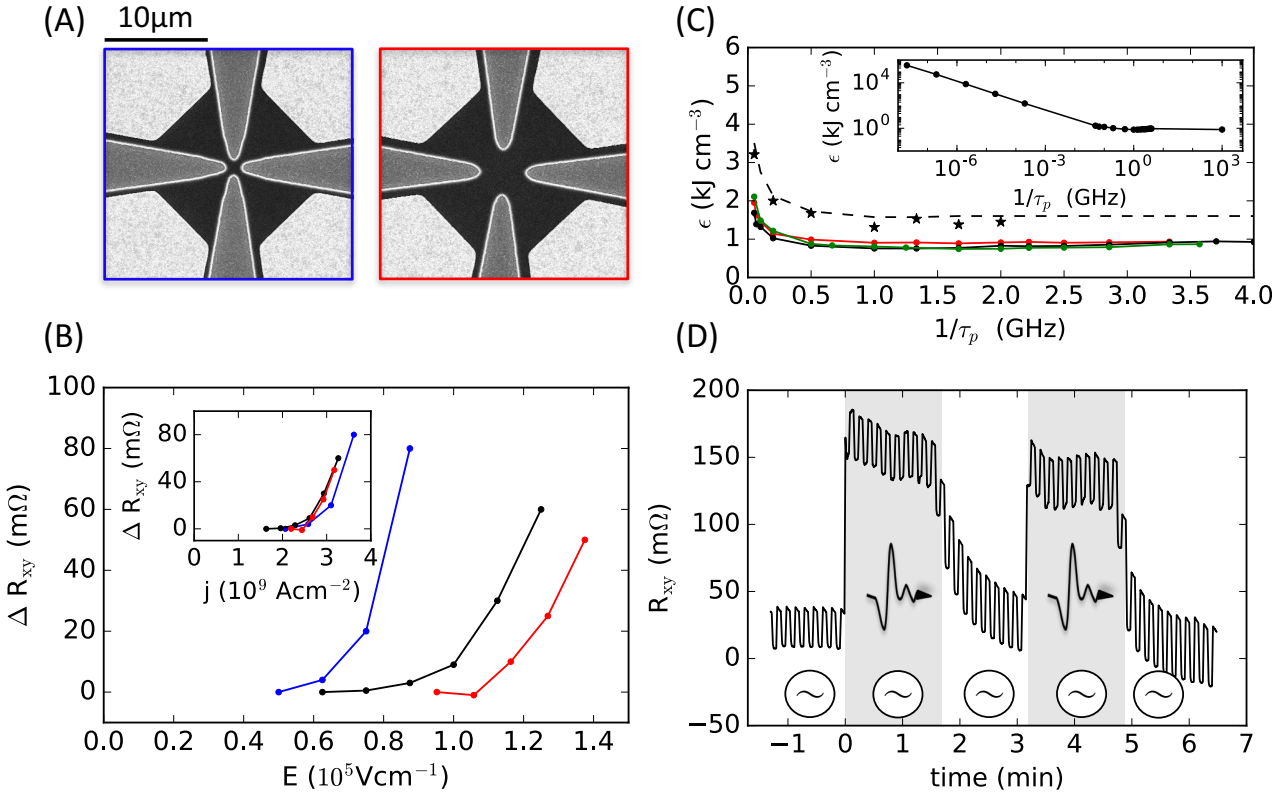

Figure 6: (A) Electron microscopy images of the 1 and 3 μm size devices. Light regions are Au-contact pads, grey regions are etched down to the GaAs substrate, and black regions are CuMnAs. (B) Magnitude of the switching signal as a function of the THz field amplitude (main panel) and of the converted current density (inset) for 1, 2 and 3 μm size devices (blue, black, and red dots). (C) Writing energy density (black, red, and green dots), $\epsilon = j^2\tau_p/\sigma$, required to obtain a 1 mΩ switching signal as a function of the writing speed $1/\tau_p$ in the linear scale (main plot) and in the log-log scale (inset). All data points, except for the point at $1/\tau_p$=1 THz in the inset are obtained from the contact measurements. The point at $1/\tau_p$=1 THz in the inset is from the non-contact measurement using the E to j conversion based on the breakdown energy (see text). Black dots in the main plot correspond to 2 μm, red to 3 μm, and green to 4 μm size CuMnAs/GaAs bit cells. Black star-symbols and dashed line represent the limiting breakdown energy density. (D) Contact writing by 200 ms pulses of current density 1×10^7 Acm^{-2} (white intervals) and the contact writing superimposed on the non-contact writing by a train of ps-pulses with a kHz repetition rate and a THz field amplitude corresponding to an additional current density of approximately 1.6×10^9 Acm^{-2} (grey intervals). Data were measured in a 10 μm-size CuMnAs/Si bit cell.

illustration we choose a CuMnAs/Si bit cell and plot the readout signal when applying 200 ms pulses of $j = 1 \times 10^7$ Acm^{-2} by the contact method with alternating orthogonal current-path directions and a delay between pulses of 5 s. After 15 switchings we added the non-contact writing in the form of a 90 s long train of ps-pulses with a kHz repetition rate and a current density $j \approx 1.6 \times 10^9$ Acm^{-2}. The non-contact ps-pulses induce an additional switching of the multi-level cell with the superimposed smaller switching signals controlled by the contact pulses.

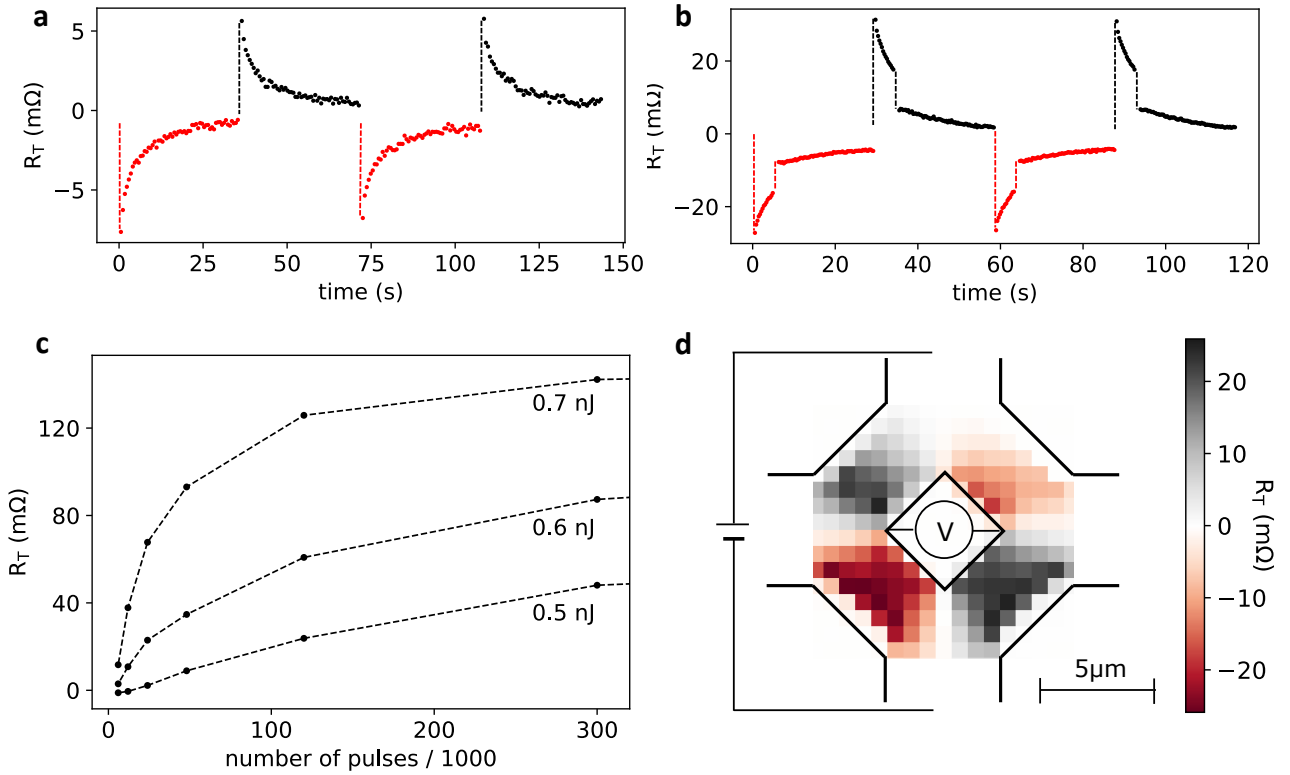

Figure 7: **Optical switching.** **a,** Electrical readout signal recorded 550 ms after optical switching by a single 100 fs, 1.7 μm-focus pulse of 1 nJ delivered to one spot on one arm (red) and one spot on the neighboring arm (black) in a bridge device with 2.5 μm wide arms. **b,** Optical writing by a laser beam of 10 kHz repetition rate over 250 ms and with 0.8 nJ per 100 fs pulse, focused to a single 1.7 μm-diameter spot in one arm (red). After 5 s, a second laser pulse was applied defocused to a 2× larger spot. The same procedure was then applied to the neighboring arm (black) in a bridge device with 5 μm wide arms. **c,** Electrical readout signal as a function of the number of 100 fs laser pulses (with energy per pulse from 0.5 to 0.7 nJ) recorded 550 ms after completing a 600 ms scan of the switching laser beam over one arm of the bridge with the repetition rate varied from 10 kHz to 0.5 MHz. **d,** Spatially resolved, pixel-by-pixel optical switching combined with electrical readout in the Wheatstone-bridge device. Each micron-size pixel was exposed to a train of pulses with a 10 kHz repetition rate over 250 ms. The beam was focused to a $\sim$ 1 μm spot and delivered energy of 0.7 nJ per 100 fs pulse. All measurements are at room temperature.

2 Switching by optical fs-pulses

To explore the ultimate pulse-length limit we now move on to the optical switching [11]. In the measurement shown in Fig. 7a we used a 800 nm wavelength laser beam with a 1.7 μm spot size and an energy of 1 nJ (30% absorbed) per 100 fs pulse. Using a pulse-picker we select a single 100 fs pulse focused on a single spot on a Wheatstone bridge device. 550 ms after the laser pulse we start recording the electrical readout signal R_T. We then shift the laser spot to the neighboring arm of the Wheatstone bridge and again perform the single-pulse switching measurement. In analogy to the electrical switching in the same device (see Report 1.3), the sign of R_T flips when shifting the spot from one to the neighboring arm and we observe the same relaxation characteristics of the signal. The energy density required for switching by the single fs-laser pulse ($\sim$kJcm^{-3}) is comparable to the Joule energy density in the electrical switching by a ns-pulse (see Fig. 8). Since switching is governed by the energy (current) density, our mechanism allows for the device scalability as in the latest generation of ferromagnetic spin-torque memories, and in contrast to the unscalable traditional magnetic recording

by the Oersted field proportional to current.

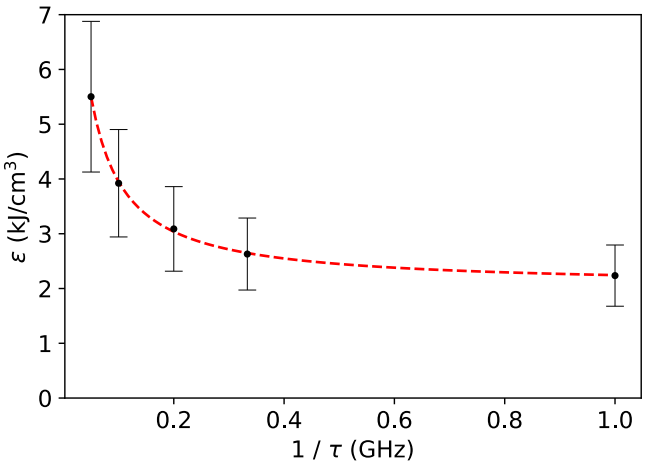

Figure 8: Joule heating energy density as a function of the switching speed $1/\tau$ (τ is the pulse length) measured on a 5 μm wide bar device. The energy density is calculated from the current density (0.9×10^8 Acm^{-2} for $\tau = 1$ ns) and resistivity during the pulse. At 200°C, the resistivity increases by a factor of 3 compared to room temperature. The error bars correspond to the estimated temperature increase during the pulse of 200 ± 50∘C. Measurements are performed close to the switching threshold with the corresponding switching signal of 1%. For comparison, switching by the single 100 fs laser pulse of energy 1 nJ with the measured 30% absorption in the sample, 1.7 μm spot size, and 50 nm film thickness (Fig. 7a) corresponds to energy density of 2.6 kJcm^{-3}. This is comparable to the saturated energy value for ns-electrical pulses.

We emphasize that only ferrimagnets with unequal demagnetization dynamics of the opposite sublattice moments were earlier argued to be switchable by a single fs-laser pulse [12], excluding the abundant family of antiferromagnets. (Note that recent demonstrations of all-optical switching in ferromagnets required, besides demagnetization, multiple circularly-polarized pulses.) Our mechanism makes switching by a single fs-laser pulse possible in antiferromagnets, and our energy in the laser pulse is lower than in the earlier all-optical switching experiments in ferrimagnets [12].

Next we show that we can optically control the high/low resistance switching. In the measurement in Fig. 7b we fixed the position of the laser spot in one arm and first applied the 1.7 μm focused laser beam with 10 kHz repetition rate over 250 ms. Then we measured for 5 s the readout signal. Next we applied another pulse train in which we defocused the beam to a 2× larger diameter to reduce its maximum energy. We observe the falling edge in the readout signal. In analogy to the electrical switching experiment discussed in the respective Report 1.3, the size of the falling edge depends on the delay between the stronger and the weaker laser pulse (see Fig. 9).

The optical switching we observe is independent of the polarization of the laser pulse, as shown in Fig. 10. The comparison between Figs. 7a,b also shows that the switching signals after a train of pulses are larger than after a single laser-pulse. The dependence on the number and amplitude of the laser pulses is studied in detail in Fig. 7c (see also Fig. 11). Here to facilitate a direct comparison to the amplitudes in the electrical switching measurements (see Report 1.3), we show the readout signal measured after completing a scan of the laser beam over the entire arm of the Wheatstone-bridge device. Using a pulse-picker, the points in Fig. 7c are obtained with a 600 ms long scanning pulse train while the repetition rate is increased from 10 kHz to 0.5 MHz. The switching signals generated by the optical pulses reach comparably high amplitudes as in the case of electrical pulses. Also in analogy to the electrical writing, we observe a multi-level optical switching but due to the high repetition rates of the laser pulses we can access orders of magnitude higher number of pulses. A single device is exposed to millions of pulses in these optical measurements which, apart from the reproducibility,

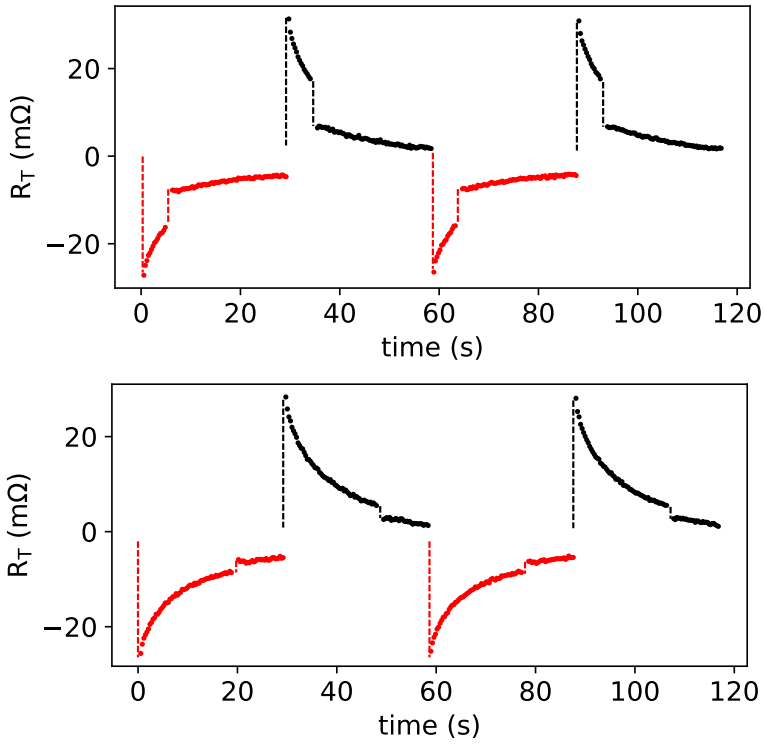

Figure 9: Optical writing by a laser beam of 10 kHz repetition rate over 250 ms and with 0.8 nJ per 100 fs pulse, focused to a single 1.7 μm-diameter spot in one arm (red). After 5 s (top panel) or 20 s (bottom panel), a second laser pulse was applied defocused to a 2× larger spot. The same procedure was then applied to the neighboring arm (black). All measurements are at room temperature.

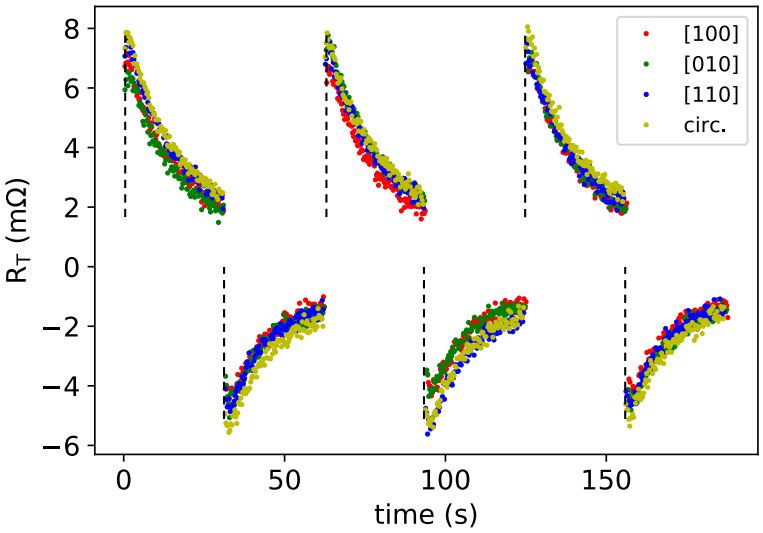

Figure 10: Switching signals measured for linearly polarized laser pulses along specified crystallographic directions in the sample, and for circularly polarized laser pulses (circ.). Experiments were performed with 0.5 nJ per pulse, 10 ms pulse train, and 80 MHz repetition rate.

evidences the endurance of the devices in our switching experiments.

To illustrate the additional spatial resolution allowed by extending our switching mechanism to optical pulses, we plot in Fig. 7d a scanning pixel-by-pixel sequence of optical-writing and electrical-

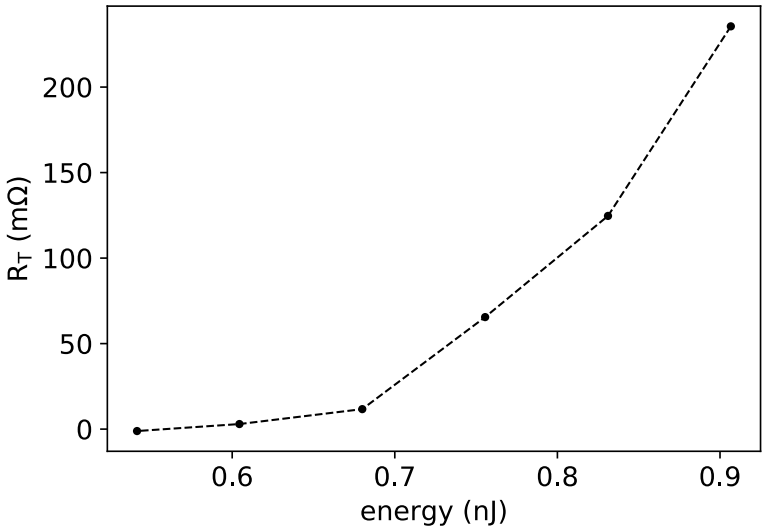

Figure 11: Dependence of the optical switching signal on the energy per 100 fs laser pulse for a 600 ms long pulse train with 10 kHz repetition rate.

readout in the Wheatstone bridge device. Here each micron-size pixel is exposed to a train of pulses with a 10 kHz repetition rate over 250 ms. Then we record the electrical readout signal R_{T} and shift the laser spot to the next pixel and repeat the same measurement procedure. As expected, the sign of the signal sharply changes when shifting the spot across the neighboring arms.

References

[1] Wadley, P. *et al.* Tetragonal phase of epitaxial room-temperature antiferromagnet CuMnAs. *Nature Communications* **4**, 2322 (2013). 1402.3624.

[2] Olejník, K. *et al.* Antiferromagnetic CuMnAs multi-level memory cell with microelectronic compatibility. *Nature Communications* **8**, 15434 (2017).

[3] Wadley, P. *et al.* Electrical switching of an antiferromagnet. *Science* **351**, 587–590 (2016). 1503.03765.

[4] Kriegner, D. *et al.* Multiple-stable anisotropic magnetoresistance memory in antiferromagnetic MnTe. *Nature Communications* **7**, 11623 (2016). 1508.04877.

[5] Grzybowski, M. J. *et al.* Imaging Current-Induced Switching of Antiferromagnetic Domains in CuMnAs. *Physical Review Letters* **118**, 057701 (2017). 1607.08478.

[6] Sajadi, M., Wolf, M. & Kampfrath, T. Terahertz-field-induced optical birefringence in common window and substrate materials. *Optics Express* **23**, 28985 (2015). URL https://www.osapublishing.org/abstract.cfm?URI=oe-23-22-28985.

[7] Kampfrath, T. *et al.* Coherent terahertz control of antiferromagnetic spin waves. *Nature Photonics* **5**, 31–34 (2011).

[8] Baierl, S. *et al.* Nonlinear spin control by terahertz-driven anisotropy fields. *Nature Photonics* **10**, 715–718 (2016).

[9] Novitsky, A. *et al.* Non-resonant terahertz field enhancement in periodically arranged nanoslits. *Journal of Applied Physics* **112**, 074318 (2012).

[10] McMahon, J. M., Gray, S. K. & Schatz, G. C. Fundamental behavior of electric field enhancements in the gaps between closely spaced nanostructures. *Physical Review B* **83**, 115428 (2011). 1008.2490.

[11] Kašpar, Z. *et al.* High resistive unipolar-electrical and fs-optical switching in a single-layer antiferromagnetic memory 1–22 (2019). URL http://arxiv.org/abs/1909.09071. 1909.09071.

[12] Kimel, A. V. & Li, M. Writing magnetic memory with ultrashort light pulses. *Nature Reviews Materials* **4**, 189–200 (2019).